International Astronautical Congress, Milan, Italy, 14-18 October 2024.

IAC-24,C1,2,8,x87662

Design of flight control systems for RLVs with structural flexibility: application to the CALLISTO vehicle

José Alfredo Macés-Hernández[a]*, **David Seelbinder**[a], **Stephan Theil**[a]

[a] *German Aerospace Center (DLR), Institute of Space Systems, Department of Guidance, Navigation and Control Systems, Robert-Hooke-Str. 7, 28359, Bremen, Germany.*
E-mails: jose.maceshernandez@dlr.de, david.seelbinder@dlr.de, stephan.theil@dlr.de

* Corresponding author

Abstract

The analysis of structural flexibility in Launch Vehicles (LVs) and Reusable Launch Vehicles (RLVs) is a vital aspect during the design and operation of the Guidance, Navigation and Control (GNC) subsystem. This aspect becomes even more critical as vehicles are currently becoming larger and slender due to conflicting goals: 1) needing larger payloads deployed into orbit and, at the same time, 2) reducing losses due to shape-induced drag. During its flight across the atmosphere, several forces acting interact with the vehicle's structure i.e., those produced by the actuators (Thrust Vector Control (TVC), Reaction Control System (RCS) and/or fins) or disturbances like the aerodynamic forces created by the body itself.

Addressing this problem from a Guidance, Navigation and Control (GNC) perspective requires an understanding of structural mechanics. This requires the usage of mechanical equivalent models that capture the core dynamics of the problem. The parameters used by practitioners are typically extracted from more accurate, but computationally expensive, methods like Finite Element Method (FEM) analysis. The high-frequency response of the vehicle is decomposed as the sum of the harmonic response of n so-called modes. Each mode is characterized by a natural frequency ω_{ni} and a modal shape Φ_j, which changes depending on the viewpoint (force application location or measurement unit location). The first and natural step is to look at the positioning of the frequencies compared to the desired rigid-body bandwidth. Furthermore, in the frequency domain, the bending modes are translated into resonances with gain amplification and phase shift, which in terms of the control systems means; correct gain and phase margins in the closed-loop must be guaranteed.

In our investigations, we perform the analysis for a real 40 KN-class vehicle, an Reusable Launch Vehicle (RLV) with a gimbaling engine, flying a typical Return-to-Launch-Site (RTLS) scenario trajectory and varying mass. First, we present the mathematical procedure to consolidate the models used for simulation and control design. Secondly, we present the evolution of the frequencies and modal shapes across the trajectory for the atmospheric ascent phase of the vehicle. Consequently, we present problem formulation from a control perspective, the n modes are introduced into the state-state representation from our earlier investigations, and later employed for control synthesis.

In the final part, the closed-loop behavior of the flight control system for the Cooperative Action Leading to Launcher Innovation for Stage Tossback Operation (CALLISTO) vehicle is validated against the influence of structural flexibility. The performance of an $\mathcal{H}_\infty$ synthesized rigid body controller from our earlier investigations, has been extended accordingly, and is validated. Monte Carlo (MC) simulations are run on the 6-Degrees of Freedom (DoF) simulator for the reference mission under nominal and uncertain conditions.

1. Introduction

Structural flexibility is a well-known issue in the space and aeronautics domains [1, 2]. Building larger and lightweight rockets, that can carry heavier payloads into orbit, usually makes them much more flexible. This phenomenon has been well studied since the first launch vehicles were developed during the sixties [3–5]. Many testing campaigns were dedicated to the correct characterization of the vehicles' structural properties.

Flexible launch vehicles [4–9] are unique systems because they are aerodynamically unstable by design, the center of pressure is forward the center of gravity. The

mass variation as the propellant consumes complicates things further, the static and dynamic parameters change, which introduces larger degrees of uncertainty into the system. The parameters used for the description of the high-frequency dynamics are also affected.

Bending modes have generally low damping, and some of the lower frequency ones could be dangerously located next to rigid body control frequency. If not correctly addressed, they can be excited by the Flight Control System (FCS) and consequently lead to instability and potential vehicle loss. To avoid this kind of issue, engineers must guarantee correct margins at low and high frequencies during the early design phase, and subsequently validate them using non-linear simulations. Generally, a design with filters is necessary to guarantee correct gain and phase.

Bending modes could be either gain or phase-stabilized [10, 11]. For phase stabilization, bending filters are used to guarantee adequate phase when in proximity with the rigid body control, while in gain stabilization the bending modes are attenuated by direct roll-off.

2. Dynamic modeling

The structural dynamics of an elastic vehicle can be studied using modal analysis. Modal analysis is a subbranch of structural mechanics that aims at determining the natural modal shapes and natural frequencies of an object during free vibration. Typical models used in structural dynamics consist of an assembly of springs and masses arranged in mesh form, connected by n discrete points called nodes.

For systems with relatively simple dynamics (made of a single material and regular form), analytical solutions can be directly computed. Newer methods, however, deal with the fact that structures are made of a combination of materials with different densities and their shapes are non-uniform and complex. Finite Element Method (FEM) analysis directly applied onto a mesh generated using the Computer-Aided Design (CAD) model state of the art within the aerospace industry [12].

Regardless of whether analytical solutions or FEM analysis is used, the goal is to find the solutions to the differential equation represented by [13]

$$\boldsymbol{M}\ddot{\boldsymbol{q}} + \boldsymbol{K}\boldsymbol{q} = \boldsymbol{\mathscr{f}}\,, \tag{1}$$

where

- $\boldsymbol{M} \in \mathbb{R}^{n\times n}$ (kg or $\mathrm{kg\,m^2\,rad^{-1}}$) is the generalized mass matrix,
- $\boldsymbol{K} \in \mathbb{R}^{n\times n}$ ($\mathrm{N\,m^{-1}}$ or $\mathrm{N\,m\,rad^{-1}}$) is the generalized stiffness matrix,
- $\boldsymbol{q} = \begin{bmatrix} q_1 & q_2 & \dots & q_n \end{bmatrix}^\top \in \mathbb{R}^{n\times 1}$ (m or rad) is the generalized displacements vector (composed of position and/or angles variables), and
- $\boldsymbol{\mathscr{f}} = \begin{bmatrix} \mathscr{f}_1 & \mathscr{f}_2 & \dots & \mathscr{f}_n \end{bmatrix}^\top \in \mathbb{R}^{n\times 1}$ (N or $\mathrm{N\,m}$) is the generalized loads vector (composed of forces and/or torques).

From a mathematical point of view, modal analysis consists of finding the general solution to differential equation (1), when the Left-Hand Side (LHS) is neglected ($\boldsymbol{M}\ddot{\boldsymbol{q}} + \boldsymbol{K}\boldsymbol{q} = \boldsymbol{0}$), i.e., the free response without external excitations is observed. Thus, one can represent it as the sum of n harmonic responses of the form

$$\boldsymbol{q}(t) = \sum_{i=1}^{n} \boldsymbol{\phi}_i\, \lambda_i\, \sin(\omega_{\mathrm{n}i}\, t + \psi_i), \quad \forall t\,, \tag{2}$$

in general, it is easier to interpret this equation when expressed in exponential form

$$\boldsymbol{q}(t) = \sum_{i=1}^{n} \boldsymbol{\phi}_i\, \lambda_i\, e^{j(\omega_{\mathrm{n}i} t + \psi_i)}, \quad \forall t\,, \tag{3}$$

where

- $\omega_{\mathrm{n}i} \in \mathbb{R}$ is the i-th natural undamped frequency ($\mathrm{rad\,s^{-1}}$),
- $\phi_i \in \mathbb{R}^n$ is the i-th modal shape (m or rad),
- $\lambda_i \in \mathbb{R}$ is the i-th gain (-), and
- $\psi_i \in \mathbb{R}$ is the i-th phase angle (rad), and

n are known as modes. Overall, only a number of the first modes is necessary since they build up most of the total response. Both, the phase and gain are not important since they depend on the initial conditions ($q_i(t_0)$ and $\dot{q}_i(t_0)$), thus they are, for most of the cases, neglected. For the computation of $\omega_{\mathrm{n}i}$ and $\boldsymbol{\phi}_i$, the solution is the result of an eigenvalue-eigenvector problem of the form

$$(\boldsymbol{M}\omega_{\mathrm{n}i}^{\,2} - \boldsymbol{K})\boldsymbol{\phi}_i = 0, \quad i = \{1, 2, \dots, n\}\,. \tag{4}$$

One needs to solve for ω_{n} in Eq. (4), i.e., $\det(\boldsymbol{M}\boldsymbol{\omega_{\mathrm{n}}}^{\,2} - \boldsymbol{K}) = \boldsymbol{0}$. n solutions will be found (i.e., $\omega_{\mathrm{n}i} = \{\omega_{\mathrm{n}1}, \omega_{\mathrm{n}2}, \dots, \omega_{\mathrm{n}n}\}$). The second step is then to find the eigenvector $\boldsymbol{\phi}_i$ that satisfies Eq. (4) for each $\omega_{\mathrm{n}i}$.

Eigenvectors $\boldsymbol{\phi}_i \in \mathbb{R}^{6\times 1}$ represent the so-called modal shape. Each modal shape is composed of a rotational $\boldsymbol{\phi}_{\mathrm{r}} \in \mathbb{R}^{3\times 1}$ and a translational $\boldsymbol{\phi}_{\mathrm{t}} \in \mathbb{R}^{3\times 1}$ parts ($\boldsymbol{\phi}_i = \begin{bmatrix} \boldsymbol{\phi}_{\mathrm{t}i}^\top & \boldsymbol{\phi}_{\mathrm{r}i}^\top \end{bmatrix}$). The n modal shape vectors can be used to

construct the modal shape matrix $\boldsymbol{\Phi} \in \mathbb{R}^{6\times n}$ for a system with n modes, i.e.,

$$\boldsymbol{\Phi} = \begin{bmatrix} \boldsymbol{\phi}_1 & \boldsymbol{\phi}_2 & \dots & \boldsymbol{\phi}_n \end{bmatrix} = \begin{bmatrix} \boldsymbol{\phi}_{\mathrm{t}1} & \boldsymbol{\phi}_{\mathrm{t}2} & \cdots & \boldsymbol{\phi}_{\mathrm{t}n} \\ \boldsymbol{\phi}_{\mathrm{r}1} & \boldsymbol{\phi}_{\mathrm{r}2} & \cdots & \boldsymbol{\phi}_{\mathrm{r}n} \end{bmatrix} \quad (\text{-}), \tag{5}$$

with

$$\boldsymbol{\phi}_{\mathrm{t}} = \begin{bmatrix} \phi_{\mathrm{t}_1} & \phi_{\mathrm{t}_2} & \phi_{\mathrm{t}_3} \end{bmatrix}^\top,$$

$$\boldsymbol{\phi}_{\mathrm{r}} = \begin{bmatrix} \phi_{\mathrm{r}_1} & \phi_{\mathrm{r}_2} & \phi_{\mathrm{r}_3} \end{bmatrix}^\top.$$

The matrix $\boldsymbol{\Phi}$ matrix is used to convert between modal and physical coordinates, its columns represent the one mode. Therefore, it is a common practice to introduce into the modal equation the mapping $\boldsymbol{q} = \boldsymbol{\Phi}\boldsymbol{\eta}$ (and its inverse transformation $\boldsymbol{\eta} = \boldsymbol{\Phi}^{-1}\boldsymbol{q}$) [1]. Or, in scalar form:

$$q_j = \sum_{i=1}^{n} \phi_{[j,i]}\, \eta\,.$$

The advantage of the modal mapping is that it reduces the number of computations. Given the fact that vector $\boldsymbol{q}$ has as units (m or rad), and knowing that eigenvectors are dimensionless, the units resulting units the modal variables will also have as units (m or rad).

Recall that the dynamics of a flexible aerospace structure can be generalized using Eq. (1)

$$\boldsymbol{M}\,\ddot{\boldsymbol{q}} + \boldsymbol{D}\,\dot{\boldsymbol{q}} + \boldsymbol{K}\,\boldsymbol{q} = \boldsymbol{\mathscr{f}}, \tag{6}$$

however, the main difference in this case, is the fact that the damping matrix ($\boldsymbol{D} \in \mathbb{R}^{n\times n}$) now has been included for energy dissipation, this matrix is a function of the structural damping coefficient ${\zeta_i}^2$, the modal mass m_i and the mode's natural frequency ω_{n_i}.

By introducing mapping $\boldsymbol{q} = \boldsymbol{\Phi}\boldsymbol{\eta}$ and pre-multiplying Eq. (6) by $\boldsymbol{\Phi}^\top$ [14], this yields to

$$\underbrace{\boldsymbol{\Phi}^\top \boldsymbol{M}\boldsymbol{\Phi}}_{\boldsymbol{M}_\eta}\ddot{\boldsymbol{\eta}} + \underbrace{\boldsymbol{\Phi}^\top \boldsymbol{D}\boldsymbol{\Phi}}_{\boldsymbol{D}_\eta}\dot{\boldsymbol{\eta}} + \underbrace{\boldsymbol{\Phi}^\top \boldsymbol{K}\boldsymbol{\Phi}}_{\boldsymbol{K}_\eta}\boldsymbol{\eta} = \boldsymbol{\Phi}^\top \boldsymbol{\mathscr{f}} \quad (\mathrm{N\ or\ N\,m}), \tag{7}$$

which for each mode is represented as

$$m_i(\ddot{\eta}_i + 2\zeta_i\omega_{\mathrm{n}_i}\dot{\eta}_i + {\omega_{\mathrm{n}_i}}^2\eta_i) = \boldsymbol{\phi}_i^\top \boldsymbol{\mathscr{f}}, \quad i = \{1, 2, \dots, n\}, \tag{8}$$

which demonstrates and interesting property of matrix $\boldsymbol{\Phi}$, it diagonalizes matrices $\boldsymbol{M}$, $\boldsymbol{D}$ and $\boldsymbol{K}$ as follows

- $\boldsymbol{M}_\eta = \boldsymbol{\Phi}^\top \boldsymbol{M}\boldsymbol{\Phi} = \mathrm{diag}\left(\begin{bmatrix} m_1 & m_2 & \dots & m_n \end{bmatrix}\right) \in \mathbb{R}^{n\times n}$ (kg or $\mathrm{kg\,m^2\,rad^{-1}}$) is the generalized masses matrix,
- $\boldsymbol{D}_\eta = \boldsymbol{\Phi}^\top \boldsymbol{D}\boldsymbol{\Phi} = 2\,\mathrm{diag}\left(\begin{bmatrix} m_1\zeta_1\omega_{\mathrm{n}1} & m_2\zeta_2\omega_{\mathrm{n}2} & \dots & m_n\zeta_n\omega_{\mathrm{n}n} \end{bmatrix}\right) \in \mathbb{R}^{n\times n}$ ($\mathrm{N\,s\,m^{-1}}$ or $\mathrm{N\,m\,s\,rad^{-1}}$) is the generalized damping matrix,
- $\boldsymbol{K}_\eta = \boldsymbol{\Phi}^\top \boldsymbol{K}\boldsymbol{\Phi} = \mathrm{diag}\left(\begin{bmatrix} m_1\,{\omega_{\mathrm{n}1}}^2 & m_2\,{\omega_{\mathrm{n}2}}^2 & \dots & m_n\,{\omega_{\mathrm{n}n}}^2 \end{bmatrix}\right) \in \mathbb{R}^{n\times n}$ ($\mathrm{N\,m^{-1}}$ or $\mathrm{N\,m\,rad^{-1}}$) is the generalized stiffness matrix.

A common practice within the structural dynamics community is to normalize the modal shape matrix wrt. the generalized mass matrix $\boldsymbol{M}_\eta$ -or the stiffness matrix-. This approach is classically employed within FEM analysis software for the retrieval of the results of the modal analysis. Both sides of Eq. (7) are pre-multiplied by ${\boldsymbol{M}_\eta}^{-1}$ [15–18], which is equivalent to scale each of the eigenvectors by the corresponding mass element

$$\hat{\boldsymbol{\phi}}_i = \frac{\boldsymbol{\phi}_i}{\sqrt{m_{\mathrm{i}}}} = \frac{\boldsymbol{\phi}_i}{\sqrt{\boldsymbol{\phi}_i^\top \boldsymbol{M}_\eta \boldsymbol{\phi}_i}} \quad (\text{-}). \quad i = \{1, 2, \dots, n\}, \tag{9}$$

Therefore the components of the matrices in Eq. (6) can be rewritten as

- $\hat{\boldsymbol{M}}_\eta = \hat{\boldsymbol{\Phi}}^\top \boldsymbol{M}\hat{\boldsymbol{\Phi}} = \mathbf{I}_{n\times n} \in \mathbb{R}^{n\times n}$ (kg or $\mathrm{kg\,m^2\,rad^{-1}}$) is the unitary modal mass matrix,
- $\hat{\boldsymbol{D}}_\eta = \hat{\boldsymbol{\Phi}}^\top \boldsymbol{D}\hat{\boldsymbol{\Phi}} = 2\,\boldsymbol{Z}_{n\times n}\boldsymbol{\Omega}_{\mathrm{n}n\times n} = 2\,\mathrm{diag}\left(\begin{bmatrix} \zeta_1\omega_{\mathrm{n}1} & \zeta_2\omega_{\mathrm{n}2} & \dots & \zeta_n\omega_{\mathrm{n}n} \end{bmatrix}\right) \in \mathbb{R}^{n\times n}$ ($\mathrm{N\,s\,m^{-1}}$ or $\mathrm{N\,m\,s\,rad^{-1}}$) is the normalized modal damping matrix, and
- $\hat{\boldsymbol{K}}_\eta = \hat{\boldsymbol{\Phi}}^\top \boldsymbol{K}\hat{\boldsymbol{\Phi}} = \boldsymbol{\Omega}^2_{\mathrm{n}n\times n} = \mathrm{diag}\left(\begin{bmatrix} {\omega_{\mathrm{n}1}}^2 & {\omega_{\mathrm{n}2}}^2 & \dots & {\omega_{\mathrm{n}n}}^2 \end{bmatrix}\right) \in \mathbb{R}^{n\times n}$ ($\mathrm{N\,m^{-1}}$ or $\mathrm{N\,m\,rad^{-1}}$) is the normalized stiffness matrix.

The normalized modal equation [16] can be represented as

[1] Eigenvectors are not orthogonal to each other, i.e., they are linearly independent. As will be shown in subsequent sections, they are, on the other hand, orthogonal to the mass and stiffness matrices.

[2] Finding structural damping of an aerospace structure is still an open field of research. This is due to the fact that modal analysis does not provide damping as a solution. Common practices include scaling it in terms of the mass, or directly selecting a value of 5% or 0.5%, for aeronautics and space applications, respectively.

$$\ddot{\boldsymbol{\eta}} + \hat{\boldsymbol{D}}_{\mathrm{B}}\dot{\boldsymbol{\eta}} + \hat{\boldsymbol{K}}_{\mathrm{B}}\boldsymbol{\eta} = \hat{\boldsymbol{\Phi}}^{\top}\boldsymbol{\not{f}}\,, \tag{10}$$

in matrix form, which for each of the modes is represented as

$$\ddot{\eta}_i + 2\,\zeta_i\,\omega_{\mathrm{n}_i}\dot{\eta}_i + \omega_{\mathrm{n}_i}^{\,2}\,\eta_i = \hat{\boldsymbol{\phi}}_i^{\top}\boldsymbol{\not{f}}\,, \quad i = \{1, 2, \ldots, n\}\,. \tag{11}$$

The modal coordinates matrix is obtained at different points, especially at those where the actuators and sensors are positioned. In a case a RLV (Fig. 1), the most important points are:

- Thrust Vector Control (TVC) gimbal $\hat{\boldsymbol{\Phi}}_{\mathrm{S}}$,
- Hybrid Navigation System (HNS) $\hat{\boldsymbol{\Phi}}_{\mathrm{N}}$,
- Fins $\hat{\boldsymbol{\Phi}}_{\mathrm{F_i}}$, with $i = \{1, 2, 3, 4\}$,
- Center of Aerodynamic Pressure (CoAP), and
- Reaction Control System (RCS)'s i-th thruster.

Since the mass of the vehicle changes as a consequence of propellant consumption, the modal shapes also change for the different filling ratios. They can be extracted from the FEM analysis software, by assuming the liquid as a solid or by using more complex techniques that also include Computer Fluid Dynamics (CFD) results in the solution.

2.1 Effect of elasticity on the sensor measurements

Structural flexibility induces parasitic vibrations that affect the sensor's measurement, depending on the placement of such sensors (accelerators, gyros), the effect propagated to the translational and rotational states of the vehicle. In the case of a launch vehicle, all the sensors are usually placed in the avionics bay. Care must be taken during the early design of the structure, such that the sensor's box is not placed at a mode's node, where the relative displacement with regard to the undeformed configuration is zero. In the specific case of CALLISTO, they are located within the HNS box which is in the top part of the vehicle [19]. For planar motion, the effect of elasticity can be included in the state-space representation using the following linear simplifications

$$\Theta_{\mathrm{N}} = \Theta - \underbrace{\sum_{i=1}^{n_f} \phi_{\mathrm{Nr_2}\,i}\,\eta_i}_{\Theta_{\mathrm{Nf}}}\,, \tag{12}$$

$$\dot{\Theta}_{\mathrm{N}} = \dot{\Theta} - \underbrace{\sum_{i=1}^{n_f} \phi_{\mathrm{Nr_2}\,i}\,\dot{\eta}_i}_{\dot{\Theta}_{\mathrm{Nf}}}\,, \tag{13}$$

$$\mathrm{x_N} = \mathrm{x} + \ell_{\mathrm{N}} - \underbrace{\sum_{i=1}^{n_f} \phi_{\mathrm{Nt_1}\,i}\,\eta_i}_{\mathrm{x_{Nf}}}\,, \tag{14}$$

$$\dot{\mathrm{x}}_{\mathrm{N}} = \dot{\mathrm{x}} - \underbrace{\sum_{i=1}^{n_f} \phi_{\mathrm{Nt_1}\,i}\,\eta_i}_{\dot{\mathrm{x}}_{\mathrm{Nf}}}\,, \tag{15}$$

$$\mathrm{y_N} = \mathrm{y} + \ell_{\mathrm{N}}\Psi - \underbrace{\sum_{i=1}^{n_f} \phi_{\mathrm{Nt_2}\,i}\,\eta_i}_{\mathrm{y_{Nf}}}\,, \tag{16}$$

$$\dot{\mathrm{y}}_{\mathrm{N}} = \dot{\mathrm{y}} + \ell_{\mathrm{N}}\dot{\Psi} - \underbrace{\sum_{i=1}^{n_f} \phi_{\mathrm{Nt_2}\,i}\,\eta_i}_{\dot{\mathrm{y}}_{\mathrm{Nf}}}\,, \tag{17}$$

$$\mathrm{z_N} = \mathrm{z} - \ell_{\mathrm{N}}\Theta - \underbrace{\sum_{i=1}^{n_f} \phi_{\mathrm{Nt_3}\,i}\,\eta_i}_{\mathrm{z_{Nf}}}\,, \tag{18}$$

$$\dot{\mathrm{z}}_{\mathrm{N}} = \dot{\mathrm{z}} - \ell_{\mathrm{N}}\dot{\Theta} - \underbrace{\sum_{i=1}^{n_f} \phi_{\mathrm{Nt_3}\,i}\,\eta_i}_{\dot{\mathrm{z}}_{\mathrm{Nf}}}\,. \tag{19}$$

These equations are quite useful when rewriting the state-space equations, which shift the output of the states from the body frame (B) to the Navigation frame (N). They were used, for instance, when extending the models from our earlier investigations [20, 21] with the modes needed for the simulation environment.

2.2 State-space representation

Assume the state-space representation of a generic 6-DoFs dynamical system is defined by

$$\dot{\boldsymbol{x}}_{\mathrm{r}} = \mathbf{A}_{\mathrm{r}}\boldsymbol{x}_{\mathrm{r}} + \mathbf{B}_{\mathrm{r}}\boldsymbol{u}\,, \tag{20}$$

$$\boldsymbol{y} = \mathbf{C}_{\mathrm{r}}\boldsymbol{x}_{\mathrm{r}} + \mathbf{D}_{\mathrm{r}}\boldsymbol{u}\,, \tag{21}$$

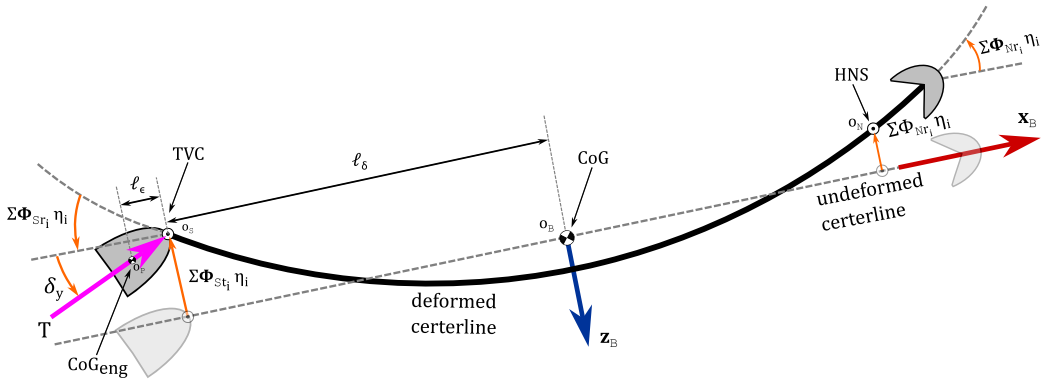

Fig. 1: Flexible launch vehicle in free-free configuration.

if this model is represented in generalized form, the states vector is organized as $\boldsymbol{x}_\mathrm{r} = \begin{bmatrix}\boldsymbol{q}_\mathrm{r} & \dot{\boldsymbol{q}}_\mathrm{r}\end{bmatrix}^\top$ for $n_x = n_{q_r} + n_{\dot{q}_r}$ states. The mapping that converts from the control inputs $\boldsymbol{u}$ to the generalized loads vector is defined by $\boldsymbol{\ell} = \mathbf{B}_\mathrm{map}\,\boldsymbol{u}$ for n_u control inputs (we will refer to the columns of this matrix as $\mathbf{B}_\mathrm{j}$, where j refers to each of the actuators generating a generalized force). Note that this approach also guarantees that the output matrix is structured as follows:

$$\mathbf{C}_\mathrm{r} = \begin{bmatrix} \mathbf{C}_{\mathrm{r}_q} & \mathbf{0}_{n_{q_r}\times n_{\dot{q}_r}} \\ \mathbf{0}_{n_{\dot{q}_r}\times n_{q_r}} & \mathbf{C}_{\mathrm{r}_{\dot{q}}} \end{bmatrix}, \tag{22}$$

$$\mathbf{D}_\mathrm{r} = \begin{bmatrix} \mathbf{0}_{n_{q_r}\times n_u} \\ \mathbf{0}_{n_{\dot{q}_r}\times n_u} \end{bmatrix}. \tag{23}$$

The state-space model from Eq. (21) can be extended with n_f flexible modes, regardless of whether they were extracted from the FEM or analytical computations. The extended state-space, which includes both the rigid body and flexible states, is

$$\begin{aligned} \begin{bmatrix} \dot{\boldsymbol{x}}_\mathrm{r} \\ \dot{\boldsymbol{x}}_\mathrm{f} \end{bmatrix} &= \left[\begin{array}{c|c} \mathbf{A}_\mathrm{r} & \mathbf{A}_\mathrm{r,f} \\ \hline \mathbf{A}_\mathrm{f,r} & \mathbf{A}_\mathrm{f} \end{array}\right] \begin{bmatrix} \boldsymbol{x}_\mathrm{r} \\ \boldsymbol{x}_\mathrm{f} \end{bmatrix} + \left[\begin{array}{c} \mathbf{B}_\mathrm{r} \\ \hline \mathbf{B}_\mathrm{f} \end{array}\right] \boldsymbol{u}\,, \\ \boldsymbol{y} &= \left[\begin{array}{c|c} \mathbf{C}_\mathrm{r} & \mathbf{C}_\mathrm{f} \end{array}\right] \begin{bmatrix} \boldsymbol{x}_\mathrm{r} \\ \boldsymbol{x}_\mathrm{f} \end{bmatrix} + \begin{bmatrix}\mathbf{D}_\mathrm{r}\end{bmatrix} \boldsymbol{u}\,, \end{aligned} \tag{24}$$

where there exist two representations for matrices $\mathbf{A}_\mathrm{f}$, $\mathbf{B}_\mathrm{f}$ and $\mathbf{C}_\mathrm{f}$, they are:

- **Generalized coordinates representation:** as the name indicates, it uses generalized coordinates for the construction of the state-space model, this explicitly requires that the states vector of the rigid body $\boldsymbol{x}_\mathrm{r}$ is also expressed in generalized form. The state vector for the flexible modes is

$$\boldsymbol{x}_\mathrm{f} = \begin{bmatrix}\boldsymbol{q}_\mathrm{f} & \dot{\boldsymbol{q}}_\mathrm{f}\end{bmatrix}^\top, \tag{25}$$

with

$$\begin{aligned} \boldsymbol{q}_\mathrm{f} &= \begin{bmatrix} q_1 & q_2 & \dots & q_{n_f} \end{bmatrix}^\top, \\ \dot{\boldsymbol{q}}_\mathrm{f} &= \begin{bmatrix} \dot{q}_1 & \dot{q}_2 & \dots & \dot{q}_{n_f} \end{bmatrix}^\top. \end{aligned}$$

Note that for the 6-DoF case, there exist 6 variables for each i-th mode, thus the length of vector $\boldsymbol{q}$ is $6 \times n_f$.

The state-space matrices [22] are defined as

$$\mathbf{A}_\mathrm{f} = \begin{bmatrix} \mathbf{0}_{n_f\times n_f} & \mathbf{I}_{n_f\times n_f} \\ -\boldsymbol{M}^{-1}\boldsymbol{K} & -\boldsymbol{M}^{-1}\boldsymbol{D} \end{bmatrix}, \tag{26}$$

$$\mathbf{B}_\mathrm{f} = \begin{bmatrix} \mathbf{0}_{n_f\times n_u} \\ \boldsymbol{M}^{-1}\mathbf{B}_{\mathrm{map_j}} \end{bmatrix}, \tag{27}$$

j represents each of the j-th control inputs, and

$$\mathbf{C}_\mathrm{f} = \begin{bmatrix} \mathbf{C}_{\mathrm{r}_q} & \mathbf{0}_{n_q\times n_{\dot{q}}} \\ \mathbf{0}_{n_{\dot{q}}\times n_f} & \mathbf{C}_{\mathrm{r}_{\dot{q}}} \end{bmatrix}. \tag{28}$$

- **Modal coordinates representation**: this second representation uses modal coordinates for the definition of the flexible states vector, each mode has two states $\boldsymbol{x}_{\eta_i} = \begin{bmatrix}\eta_i & \dot{\eta}_i\end{bmatrix}^\top$, or

$$\begin{aligned} \boldsymbol{x}_\mathrm{f} &= \begin{bmatrix} \boldsymbol{x}_{\eta_1} & \boldsymbol{x}_{\eta_2} & \dots & \boldsymbol{x}_{\eta_{n_f}} \end{bmatrix}^\top, && (29) \\ &= \begin{bmatrix} \eta_1 & \dot{\eta}_1 & \eta_2 & \dot{\eta}_2 & \dots & \eta_{n_f} & \dot{\eta}_{n_f} \end{bmatrix}^\top, && (30) \end{aligned}$$

and the state-space matrices [22] are defined as follows

$$\mathbf{A}_{\mathrm{f}} = \begin{bmatrix} \mathbf{A}_{\eta 1} & \mathbf{0}_{2\times 2} & \cdots & \mathbf{0}_{2\times 2} \\ \mathbf{0}_{2\times 2} & \mathbf{A}_{\eta 2} & \cdots & \mathbf{0}_{2\times 2} \\ \vdots & \vdots & \ddots & \vdots \\ \mathbf{0}_{2\times 2} & \mathbf{0}_{2\times 2} & \cdots & \mathbf{A}_{\eta n_f} \end{bmatrix}, \tag{31}$$

$$\mathbf{B}_{\mathrm{f}} = \begin{bmatrix} \mathbf{B}_{\eta 1} \\ \mathbf{B}_{\eta 2} \\ \vdots \\ \mathbf{B}_{\eta n_f} \end{bmatrix}, \tag{32}$$

$$\mathbf{C}_{\mathrm{f}} = \begin{bmatrix} \mathbf{C}_{\eta 1} & \mathbf{C}_{\eta 2} & \cdots & \mathbf{C}_{\eta n_f} \end{bmatrix}, \tag{33}$$

with

$$\mathbf{A}_{\eta i} = \begin{bmatrix} 0 & 1 \\ -{\omega_{\mathrm{n}}}_i^2 & -2\zeta_i \omega_{\mathrm{n}i} \end{bmatrix},$$

$$\mathbf{B}_{\eta i} = \begin{bmatrix} \mathbf{0}_{1\times n_u} \\ \hat{\boldsymbol{\phi}}_i^{\top} \mathbf{B}_{\mathrm{map_j}} \end{bmatrix},$$

$$\mathbf{C}_{\eta i} = \begin{bmatrix} \mathbf{C}_{\mathrm{r}_q} \hat{\boldsymbol{\phi}}_i & \mathbf{0}_{n_q\times 1} \\ \mathbf{0}_{n_{\dot{q}}\times 1} & \mathbf{C}_{\mathrm{r}_{\dot{q}}} \hat{\boldsymbol{\phi}}_i \end{bmatrix},$$

note that the modal shapes $\boldsymbol{\phi}$ defined in the $\mathbf{C}$ matrices are always the modal shapes at the measurement unit, while the ones defined in the $\mathbf{B}$ matrices are at the locations of the j-th control inputs.

For the coupling matrices $\mathbf{A}_{\mathrm{r,f}}$ and $\mathbf{A}_{\mathrm{f,r}}$ we look at the values of generalized forces deviation purely due to the effect of the bending. In general, $\mathbf{A}_{\mathrm{f,r}_i} = [\mathbf{0}_{2\times n_q}]$ and

$$\mathbf{A}_{\mathrm{r,f}_i} = \begin{bmatrix} \mathbf{0}_{n_q\times 1} & \mathbf{0}_{n_q\times 1} \\ \mathbf{A}_{\mathrm{f,act}_i} & \mathbf{0}_{n_q\times 1} \end{bmatrix},$$

where

$$\mathbf{A}_{\mathrm{f,act}_i} = \begin{bmatrix} \sum_{k=1}^{j} \hat{\phi}_{j,i_1} B_{\mathrm{map}\,j_1} \\ \vdots \\ \sum_{k=1}^{j} \hat{\phi}_{j,i_{qn}} B_{\mathrm{map}\,j_{qn}} \end{bmatrix}.$$

The full-order matrices are hence expressed as

$$\mathbf{A}_{\mathrm{r,f}} = \begin{bmatrix} \mathbf{A}_{\mathrm{r,f}1} & \mathbf{A}_{\mathrm{r,f}2} & \cdots & \mathbf{A}_{\mathrm{r,f}n_f} \end{bmatrix}, \tag{34}$$

and

$$\mathbf{A}_{\mathrm{f,r}} = \begin{bmatrix} \mathbf{A}_{\mathrm{f,r}1} \\ \mathbf{A}_{\mathrm{f,r}2} \\ \cdots \mathbf{A}_{\mathrm{f,r}n_f} \end{bmatrix}. \tag{35}$$

The implementation of the state-space models for planar ascent flight is defined as a function of the state's vector

$$y_{\mathrm{r_{hns}}} = \begin{bmatrix} \Theta_{\mathrm{N}} & \dot{\Theta}_{\mathrm{N}} & \mathrm{x}_{\mathrm{o_N}} & \mathrm{z}_{\mathrm{o_N}} & \dot{\mathrm{x}}_{\mathrm{o_N}} & \dot{\mathrm{z}}_{\mathrm{o_N}} \end{bmatrix}^{\top} \tag{36}$$

for the pitch plane. And for the yaw plane as a function of states

$$y_{\mathrm{r_{hns}}} = \begin{bmatrix} \Psi_{\mathrm{N}} & \dot{\Psi}_{\mathrm{N}} & \mathrm{x}_{\mathrm{o_N}} & \mathrm{y}_{\mathrm{o_N}} & \dot{\mathrm{x}}_{\mathrm{o_N}} & \dot{\mathrm{y}}_{\mathrm{o_N}} \end{bmatrix}^{\top}. \tag{37}$$

For the analytical definition of the rigid body matrices, the reader is referred to references [20, 21], the state-space from those references can be extended using the formulation presented along this section, leading to a model that can be used for control design and analysis.

3. Application to the CALLISTO mission

The details of the CALLISTO mission can be found in other references [19–21, 23–26]. For this publication, we analyze one of the baseline scenarios (the Return-to-Launch-Site flight), the profile of this mission is depicted in Fig. 2, where all four phases composing the end-to-end flight are shown (namely, ascent, boostback, aerodynamic reentry, and landing). Each of them uses different control and guidance strategies [20, 21, 23, 24].

The modal parameters of the vehicle were extracted using FEM analysis, and accordingly depicted in Fig. 3 for only the first three actual bending modes. Although there exists data from all the force application points, for the scope of this publication, only the ones corresponding to the TVC gimbal and the HNS are computed for a portion of the ascent flight. All the parameters were also normalized regarding their maximum value due to proprietary reasons.

The parameters shown in Fig. 3 have been substituted in the model presented in Eqs. (21), and (24) and all the parameters derived across Sec. 2.2 for a rigid body with control inputs vector $\boldsymbol{u} = \begin{bmatrix} \mathsf{T} & \delta_y & \delta_\theta & v_{\mathrm{W}} \end{bmatrix}^{\top}$ for the pitch plane and $\boldsymbol{u} = \begin{bmatrix} \mathsf{T} & \delta_z & \delta_\psi & v_{\mathrm{W}} \end{bmatrix}^{\top}$ for the yaw plane. The progression of the open-loop poles and zeros is illustrated in Fig. 4's upper plot for a large section of the ascent phase, here the results only for the pitch plane poles are depicted. The state-space representation also provides the open-loop transfers for channels that are important for the vehicle,

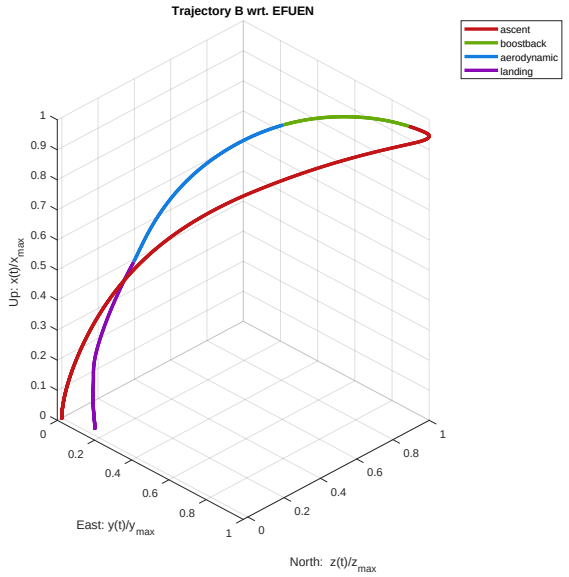

Fig. 2: CALLISTO'S flight phases for Return-to-Launch-Site (RTLS) scenario.

namely; $\frac{\Theta(\mathcal{S})}{\delta_y(\mathcal{S})}$, $\frac{\Theta(\mathcal{S})}{\delta_\theta(\mathcal{S})}$, $\frac{z(\mathcal{S})}{\delta_y(\mathcal{S})}$, $\frac{z(\mathcal{S})}{\delta_\theta(\mathcal{S})}$, $\frac{\Psi(\mathcal{S})}{\delta_z(\mathcal{S})}$, $\frac{\Psi(\mathcal{S})}{\delta_\psi(\mathcal{S})}$, $\frac{y(\mathcal{S})}{\delta_z(\mathcal{S})}$ and $\frac{y(\mathcal{S})}{\delta_\psi(\mathcal{S})}$, just to mention classically analyzed ones in the domains of launcher's control. In Fig. 4's lower plot the bode chart for the channel $\frac{\Theta(\mathcal{S})}{\delta_y(\mathcal{S})}$ for the same segment of the baseline trajectory as also depicted in Fig. 2. 20 points were evenly selected and only the first six lower frequency modes were analyzed.

Since it is also important to know how the uncertainties in the rigid and flexible body deviate from the nominal dynamics, across all the linearization points besides computing Linear Time-Invariant (LTI) systems (nominal) the Linear Fractional Transformation (LFT) systems (uncertain) were also obtained, with the baseline and uncertainty envelope, accordingly.

In the launch vehicle's ascent control, the most critical point is the maximum dynamic pressure region, here referred to as $Q_{\max}$, this is the trajectory segment where the aerodynamic forces are the largest, thus small deviation from the nominal parameters can produce very large variations on the dynamics of the system. This pole-zero map and bode plot is presented for the pitch channel ($\frac{\Theta(\mathcal{S})}{\delta_y(\mathcal{S})}$) at $Q_{\max}$ on the LFT in Fig. 5. For this analysis, the first 6 modes were selected. Here, one observes the classic aerodynamic unstable pole related to the position channel, and the pair of aerodynamic stable and unstable poles associated with the attitude channel. Furthermore, the complex poles linked to the bending modes are all contained within the LHS of the complex plane, and consequently, also stable under perturbed conditions. This is confirmed by looking at the bode plot, where the magnitude of the modes is well below 0 dB. As for the frequency separation, the poles are well separated from the frequencies of the aerodynamic poles. In terms of order magnitude, the desired rigid body Closed-Loop (CL) will be placed more than 1 decade below the lowest frequency mode.

Given the favorable gain of the modes, one could directly use a low-pass filter to roll them off and correct the phase of the system. However, a good practice is to filter at least the first one, aiming at minimizing the interaction with the rigid body, this is done by directly placing a transfer function of a notch filter of the form

$$\mathcal{G}_{\text{filter,notch}_{\text{nom}\,i}}(\mathcal{S}) = \frac{\mathcal{S}^2 + w_f\mathcal{S} + \omega_f^2}{\mathcal{S}^2 + \frac{w_f}{a_f}\mathcal{S} + \omega_f^2}\,, \tag{38}$$

directly at the output of the controller, w_f defines the width of the filter and a_f the attenuation/amplification at the given frequency ω_f for the nominal case. To handle the uncertainties in the bending parameters, usually, $\mathcal{G}_{\text{filter,notch}_{\text{rob}\,i}}(\mathcal{S})$ is composed of at least three sub-filters to attenuate the entire range of frequencies produced by parameters dispersion in the LFT, i.e.,

$$\mathcal{G}_{\text{filter,notch}_{\text{rob}\,i}}(\mathcal{S}) = \prod_{j=1}^{3} \mathcal{G}_{\text{filter,notch}_{\text{nom}\,i_j}}(\mathcal{S})\,, \tag{39}$$

where the frequencies are selected: $\omega_{f_{i_1}}$ is the lower frequency observed in the LFT for the 1-st mode, $\omega_{f_{i_2}}$ is the nominal frequency in the LTI for the first mode, and $\omega_{f_{i_3}}$ is the maximum frequency observed in the LFT also for the first mode. For our design i=1. Note that classic notch filters do not induce changes in the phase of the closed-loop system, they mostly operate on the magnitude of the system. For this reason, to recover the initial 180° at low frequencies, second-order low-pass filters are also employed to correct the phase. These low-pass filters are basic second-order filters, whose transfer is represented by

$$\mathcal{G}_{\text{filter,low}_i}(\mathcal{S}) = \frac{k_f\omega_f^2}{\mathcal{S}^2 + 2\zeta_f\omega_f + \omega_f^2}\,. \tag{40}$$

The final design for the robust design will then have the form

$$\mathcal{G}_{\text{filter,tot}}(\mathcal{S}) = \mathcal{G}_{\text{filter,notch}_{\text{rob}}}(\mathcal{S}) \cdot \prod_{i=1}^{n} \mathcal{G}_{\text{filter,low}_i}(\mathcal{S})\,. \tag{41}$$

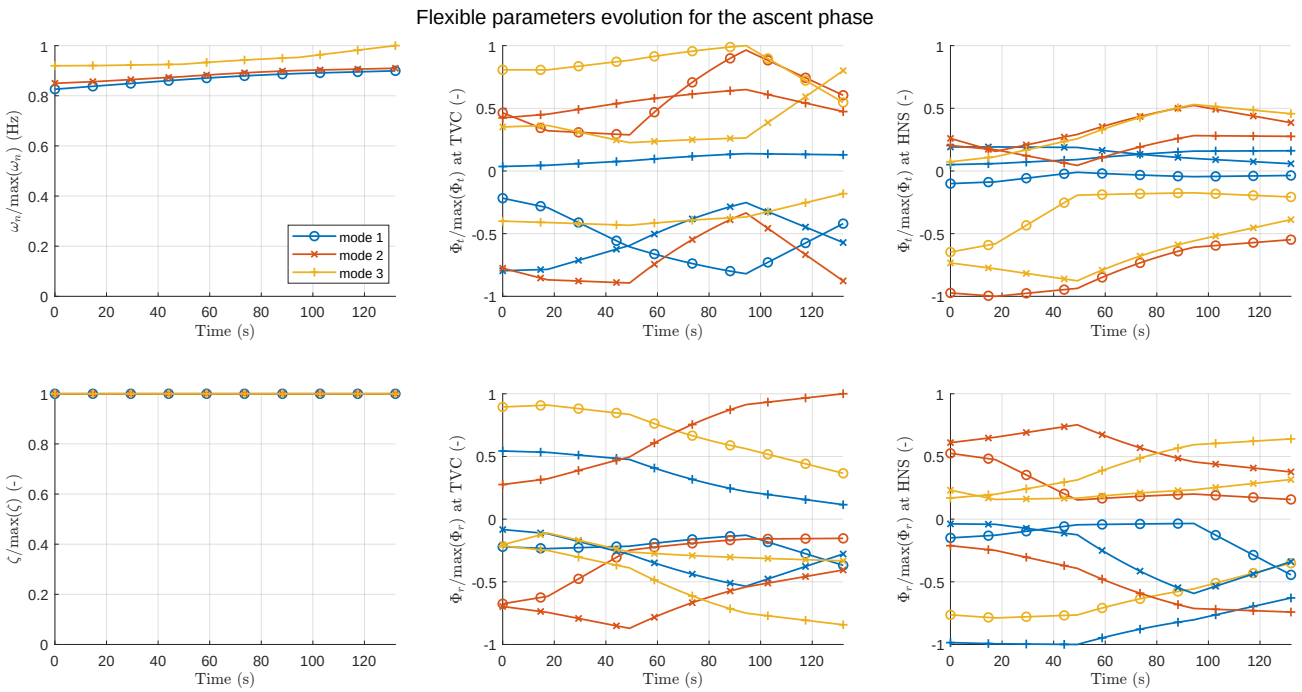

Fig. 3: Evolution of the bending parameters across the atmospheric-ascent phase for the first 3 modes.

For the computation of the control gains using $\mathcal{H}_\infty$ optimization, the structure of the controller is preserved as of [20], the total bending filter (41) is placed directly at the output of the controller. Since the structure of the filter is also fixed for all the trajectory design points, the coeffi-

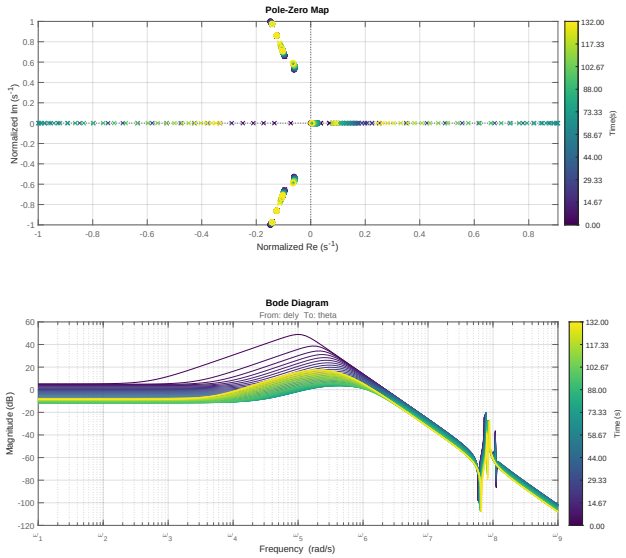

Fig. 4: Evolution of the stability parameters in open-loop across the trajectory.

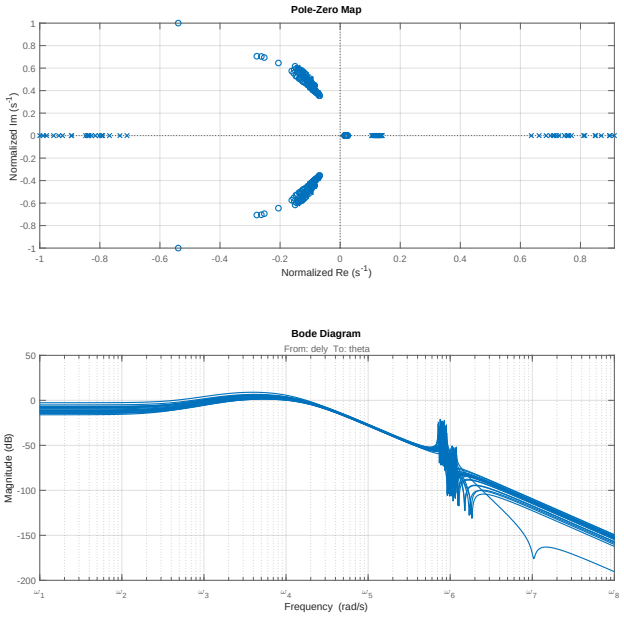

Fig. 5: Evolution of the stability parameters in open-loop at $Q_{\max}$.

cients filter transfers can be scheduled as the control gains, using the non-gravitation velocity as the independent variable for the interpolations in between points. The current design iterates over a set of n design points across the trajectory (Fig. 2), both under nominal and perturbed conditions. Classic stability margins from control theory are imposed into the rigid body, they are 6 dB for the gain margin and 30° for the phase margin, for the high-frequency dynamics, 12 dB and 45° for the nominal design. For the robust performance, these values were relaxed. The Nichols plot of the response of the current nominal system ($\mathcal{L}(s)$) is presented in Fig. 6, the same design procedure was done for each design point, guaranteeing adequate nominal and robust margins. Note that also the same design procedure is repeated both for pitch and yaw planes.

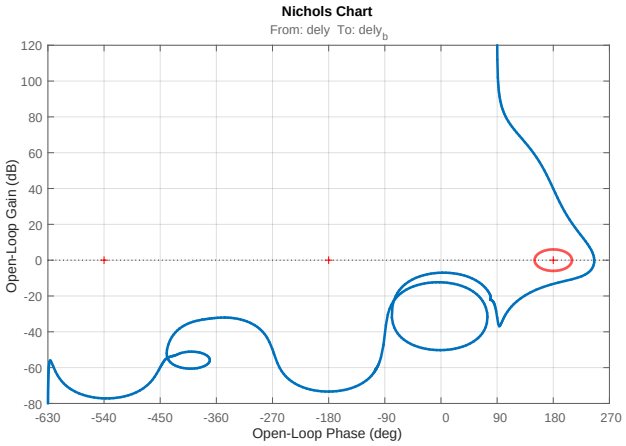

Fig. 6: Closed-loop Nichols plot for the nominal system at $Q_{\max}$.

For the closure of this publication, the design was tested in the 6DoF simulator against nominal and perturbed conditions. The simulator includes a high-fidelity model of the CALLISTO vehicle with all the bending models using the formulations presented in Sec. 2.2 and the corresponding uncertainties for the parameters that are affected. Other models included in the simulation framework include Mass, Centering, Inertia (MCI) variation, a fully ad-hoc aerodynamic model, actuator models with non-linearities, the environmental models with the wind profiles for the launch site, and communication delays between subsystems and computers. All these parameters are randomly sampled according to the probability distribution for n runs. The closed-loop performance of the nominal 6-DoF simulation with nominal wind profile is presented in Fig. 7 for the ascent phase. As expected from the Open-Loop (OL) analysis, the modes are well-damped in CL.

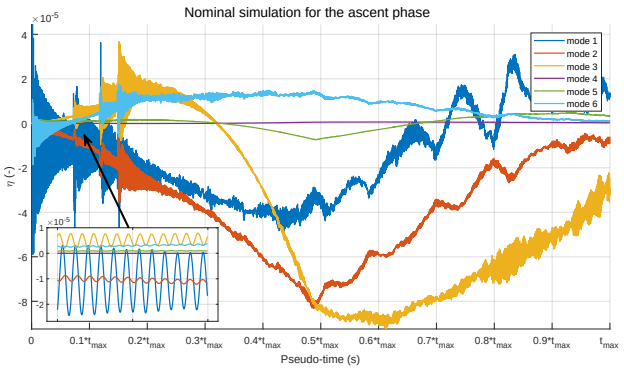

Fig. 7: Shape of the 6 first modes for nominal simulation.

The final part includes 100 runs extracted from a larger MC under perturbed conditions with randomly sampled wind profiles. In this instance, the results are shown in Fig. 8. The oscillations' amplitude is well-bounded for all the MC runs. It is also evident that there are no couplings with other effects, such as sloshing, wind, or the engine. As for compliance with the requirements of attitude/position tracking and loads minimization, they all fall well within the design requirements.

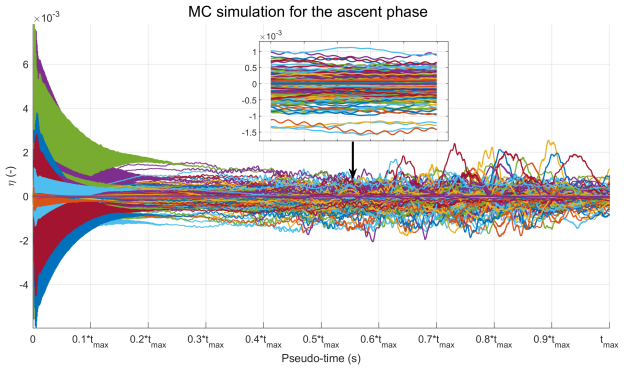

Fig. 8: Shape of all the modes for 100 MC runs.

4. Conclusions

In this publication, the modeling and analysis of structural flexibility has been analyzed for generic Launch Vehicle (LV) and RLVs. We tackled the problem in the classic fashion tailored for GNC systems.

In the first part, we introduced the computation of the modal equations that can be used both for simulation and stability analysis purposes. The process of deriving the modal coordinates in the two common representations from structural dynamics was also thoroughly discussed.

They are: 1) generalized coordinates and 2) modal coordinates. One or the other might be more useful depending on the application, classically in the launcher domain the latter is preferred. The process of extending the models that are typically used for rigid-body analysis ($\mathcal{G}_{\text{rigid}}(s)$) with unstable aerodynamic poles and sets of actuators found in conventional vehicles like TVC, RCS, or less conventional like fins cover the full spectrum of modern LVs and RLVs.

The state space representation of the i-th flexible mode can be constructed as a standalone state-space system $\mathcal{G}_{\text{flex}}(s)$ and later coupled to the rigid body via the state-coupling matrices that lead to a full order extended model suitable for control design purposes.

In the second part, the evolution of the bending parameters for the CALLISTO vehicle has been analyzed in open-loop for the ascent phase of a RTLS trajectory. The location of the bending modes frequencies relative to the aerodynamic poles has been studied at the $Q_{\max}$ under uncertain conditions along the reference trajectory for each analysis point.

The findings from the open-loop analysis defined the filter architecture used to counteract the effects of flexibility both in magnitude and phase. The current design uses a combination of notch and low pass filters to ensure adequate gain and phase margins at low and high frequencies.

In the final part, the design was validated using non-linear simulations with the high-fidelity simulator for nominal and perturbed conditions using different wind profiles. The behavior of the modes was, as expected, correctly damped and showed no couplings with other effects, like sloshing, wind, or engine dynamics.

Acknowledgments

The authors of this paper would like thank the fruitful discussions with our colleagues from the GNC department of the German Aerospace Center (DLR) in Bremen, as well as our colleagues from other DLR institutes, JAXA and CNES; who have directly and indirectly contributed to the improvement of this manuscript.

References

[1] John L. Junkins and Youdan Kim. *Introduction to Dynamics and Control of Flexible Structures*. AIAA Education Series. American Institute of Aeronautics and Astronautics, Washington, D.C, 1993.

[2] Leonardo Mazzini. *Flexible Spacecraft Dynamics, Control and Guidance*. Springer Aerospace Technology. Springer International Publishing, Cham, 2016.

[3] Nathan L Beard. A Theoretical Investigation of the Effects of the Configurative Design of a Space Vehicle on its Structural Bending Frequencies and Aerodynamic Stability. Technical Report 19630010313, National Aeronautics and Space Administration, 1962.

[4] David R. Lukens, Alfred F. Schmitt, and George T. Broucek. Approximate transfer functions for flexible-booster-and autopilot analysis. Technical report, General Dynamics Coorporation, April 1961.

[5] W. Haeussermann. Guidance and Control of Saturn Launch Vehicles. In *2nd Annual Meeting*, San Francisco, CA, U.S.A., July 1965. American Institute of Aeronautics and Astronautics.

[6] Clement Benoit. *Synthese Multiobjectifs et Sequencement de Gains : Application Au Pilotage d'un Lanceur Spatial*. PhD thesis, Université Paris XI, January 2001.

[7] Wei Du. *Dynamic Modeling and Ascent Flight Control of Ares-I Crew Launch Vehicle*. PhD thesis, Iowa State University, 2010.

[8] Jeb S. Orr, John H. Wall, Tannen S. VanZwieten, and Charles E. Hall. Space Launch System Ascent Flight Control Design. In *2014 American Astronautical Society (AAS) Guidance, Navigation, and Control Conference*, Breckenridge, CO, January 2014.

[9] Diego Navarro-Tapia. *Robust and Adaptive TVC Control Design Approaches for the VEGA Launcher*. PhD thesis, University of Bristol, 2019.

[10] A.L. Greensite. *Analysis and Design of Space Vehicle Flight Control Systems. Control Theory: Volume I.* Control Theory. Spartan Books, 1970.

[11] NASA Space Vehicle Design Criteria (Guidance and Control). Effects of structural flexibility on launch vehicle control systems. NASA Technical Report NASA SP- 8036, NASA, February 1970.

[12] Michael R. Hatch. *Vibration Simulation Using MATLAB and ANSYS*. Chapman & Hall/CRC, Boca Raton, 2001.

[13] C.W. de Silva. *Vibration: Fundamentals and Practice*. Taylor & Francis, second edition, 2006.

[14] Randall Allemang and Peter Avitabile, editors. *Handbook of Experimental Structural Dynamics*. Springer New York, New York, NY, 2022.

[15] Jimin He and Zhi-Fang Fu. *Modal Analysis*. Butterworth-Heinemann, Oxford ; Boston, 2001.

[16] Ahmed Shabana. *Vibration of Discrete and Continuous Systems*. Mechanical Engineering Series. Springer International Publishing, Cham, 2019.

[17] Jan Robert Wright and Jonathan Edward Cooper. *Introduction to Aircraft Aeroelasticity and Loads*, volume 20. John Wiley & Sons, 2008.

[18] Anil K. Chopra. *Dynamics of Structures: Theory and Applications to Earthquake Engineering*. Prentice Hall, Upper Saddle River, NJ, 4th ed edition, 2015.

[19] Etienne Dumont, Shinji Ishimoto, Pascal Tatiossian, Josef Klevanski, Bodo Reimann, Tobias Ecker, Lars Witte, Johannes Riehmer, Marco Sagliano, Sofia Giagkozoglou, Ivaylo Petkov, Waldemar Rotärmel, René Schwarz, David Seelbinder, Markus Markgraf, Jan Sommer, Dennis Pfau, and Hauke Martens. CALLISTO: A Demonstrator for Reusable Launcher Key Technologies. *Transactions of the Japan Society for Aeronautical and Space Sciences, Aerospace Technology Japan*, 19(1):106–115, January 2021.

[20] Jose Alfredo Maces Hernandez, Marco Sagliano, Ansgar Heidecker, David Seelbinder, Markus Schlotterer, Stefano Fari, Stephan Theil, Svenja Woicke, and Etienne Dumont. Ascent Flight Control System for Reusable Launch Vehicles: Full Order and Structured H∞ Designs. In *11th International ESA Conference on Guidance, Navigation & Control Systems*, Sopot, Poland, June 2021.

[21] Jose Alfredo Maces Hernandez, David Seelbinder, and Stephan Theil. Modeling and Stability Analysis of Sloshing on Liquid-Propelled Reusable Launch Vehicles. In *Aerospace Europe Conference 2023: 10th EUCASS - 9th CEAS*, Lausanne, Switzerland, July 2023.

[22] Wodek K. Gawronski. *Advanced Structural Dynamics and Active Control of Structures*. Mechanical Engineering Series. Springer-Verlag, New York, 2004.

[23] Marco Sagliano, Taro Tsukamoto, Jose Alfredo Maces Hernandez, David Seelbinder, Shinji Ishimoto, and Etienne Dumont. Guidance and Control Strategy for the CALLISTO Flight Experiment. In *8th EUCASS CONFERENCE FOR AERONAUTICS AND AEROSPACE SCIENCES*, Madrid, Spain, July 2019. EUCASS Association.

[24] Marco Sagliano, José A. Macés Hernández, Stefano Farì, Ansgar Heidecker, Markus Schlotterer, Svenja Woicke, David Seelbinder, Sven Krummen, and Etienne Dumont. Unified-Loop Structured H-Infinity Control for Aerodynamic Steering of Reusable Rockets. *Journal of Guidance, Control, and Dynamics*, 46(5):815–837, 2023.

[25] Shinji Ishimoto, Pascal Tatiossian, and Etienne Dumont. Overview of the CALLISTO Project. In *32nd ISTS and NSAT*, Fukui, Japan, June 2019.

[26] Etienne Dumont, Shinji Ishimoto, Michel Illig, Marco Sagliano, Marco Solari, Tobias Ecker, Hauke Martens, Sven Krummen, Jean Desmariaux, Yasuhiro Saito, Moritz Ertl, Josef Klevanski, Bodo Reimann, Svenja Woicke, René Schwarz, David Seelbinder, Markus Markgraf, Johannes Riehmer, Benjamin Braun, and Moritz Aicher. CALLISTO: Towards reusability of a rocket stage: Current status. In *33rd ISTS Conference*, Beppu, Japan, March 2022.